

Hybrid Far- and Near-Field Channel Estimation for THz Ultra-Massive MIMO via Fixed Point Networks

Wentao Yu, Yifei Shen, Hengtao He, Xianghao Yu, Jun Zhang, *Fellow, IEEE*, and Khaled B. Letaief, *Fellow, IEEE*

Dept. of ECE, The Hong Kong University of Science and Technology, Kowloon, Hong Kong

Email: {wyuaq, yshenaw}@connect.ust.hk, {eehthe, eexyu, eejzhang, eekhaled}@ust.hk

Abstract—Terahertz ultra-massive multiple-input multiple-output (THz UM-MIMO) is envisioned as one of the key enablers of 6G wireless systems. Due to the joint effect of its array aperture and small wavelength, the near-field region of THz UM-MIMO is greatly enlarged. The high-dimensional channel of such systems thus consists of a stochastic mixture of far and near fields, which renders channel estimation extremely challenging. Previous works based on uni-field assumptions cannot capture the hybrid far- and near-field features, thus suffering significant performance loss. This motivates us to consider hybrid-field channel estimation. We draw inspirations from fixed point theory to develop an efficient deep learning based channel estimator with adaptive complexity and linear convergence guarantee. Built upon classic orthogonal approximate message passing, we transform each iteration into a contractive mapping, comprising a closed-form linear estimator and a neural network based non-linear estimator. A major algorithmic innovation involves applying fixed point iteration to compute the channel estimate while modeling neural networks with arbitrary depth and adapting to the hybrid-field channel conditions. Simulation results verify our theoretical analysis and show significant performance gains over state-of-the-art approaches in the estimation accuracy and convergence rate. Source code is publicly available on [Github](#).

I. INTRODUCTION

Terahertz (THz) band is the last piece of the radio frequency (RF) spectrum puzzle for wireless systems [1], [2]. The massive bandwidth promises to provide ultra-high data rates and seamlessly support new applications in 6G such as extended reality, autonomous driving, and edge intelligence [3]. At the same time, many problems, such as the limited coverage range, are yet to be solved to fully unleash its potential. To combat the coverage problem in an energy-efficient manner, ultra-massive multiple-input multiple-output (UM-MIMO) with an array-of-subarray (AoSA) structure has been proposed as a promising solution [1], [4]. This structure groups the antenna array into multiple subarrays, each powered by one RF chain, to perform highly directional hybrid beamforming [5], [6]. The fine-grained feature of beamforming design necessitates accurate channel estimation with a low pilot overhead, which, however, is extremely challenging due to limited RF chains.

Conventional wireless systems operating at sub-6 GHz and millimeter wave bands mostly considered the far-field region only, as the radius of the near-field region, determined by the Rayleigh distance, is much smaller compared with the coverage range. By contrast, for THz UM-MIMO, the near-field region becomes critical due to the enlarged Rayleigh distance, which, for example, is about 20 m for an array with 0.1 m

aperture at 300 GHz. This will occupy a large portion of the coverage of a typical THz system. Therefore, depending on the distances between the RF source/scatterers and the array, far- and near-field paths typically co-exist and together constitute the hybrid-field channel. Considering such a unique feature, channel estimation algorithms for THz UM-MIMO have to be compatible with both the far- and near-field paths, and be robust against the variable channel conditions.

Unfortunately, so far there is no unified algorithm that can address these challenges. To reduce pilot overhead, existing works mostly adopted the uni-field assumption and exploited dedicated sparsity patterns in either the far field [7], [8] or near field [9] to design efficient compressed sensing algorithms. A hybrid-field scenario was considered in [10], but the authors assumed *a priori* knowledge of whether each path is from the far- or near-field region to decide what algorithm to apply, which is far from practical. As an alternative, deep unfolding (DU) methods can be adopted to learn the complex channel conditions by augmenting classic iterative algorithms with learnable components [11], [12], [13], [14], [15]. Nevertheless, several critical problems remain unsolved and hinder their application. Specifically, although adapted from classic algorithms, the convergence of DU methods is generally not guaranteed. In addition, DU methods are truncated to a *fixed* number of iterations. This contradicts the property of classic iterative algorithms and can lead to an unstable performance in the changeable channel conditions.

To tackle these issues, we develop a deep learning based hybrid-field channel estimator for THz UM-MIMO that enjoys convergence guarantee and adaptive complexity. Specifically, inspired by fixed point theory [16], we transform each iteration of orthogonal approximate message passing (OAMP) [17] into a contractive mapping, by replacing the nonlinear estimator with a specially-trained convolutional neural network (CNN). Thanks to the powerful modeling capacity of CNNs, the patterns of the hybrid-field THz UM-MIMO channel can be accurately identified and exploited. The estimated channel is computed via a fixed point iteration of the contractive mapping. It is shown that the proposed estimator enjoys provable linear convergence and can model neural networks with the depth that adapts to the hybrid-field channel conditions and an adjustable error tolerance. Simulation results will verify our theoretical results and demonstrate that the proposed method outperforms state-of-the-art approaches by a large margin.

Notation: Throughout this paper, \mathbf{A}^T , \mathbf{A}^H , \mathbf{A}^\dagger , $\text{tr}(\mathbf{A})$, $\text{vec}(\mathbf{A})$, and $(\mathbf{A})_{i,j}$ are respectively the transpose, Hermitian,

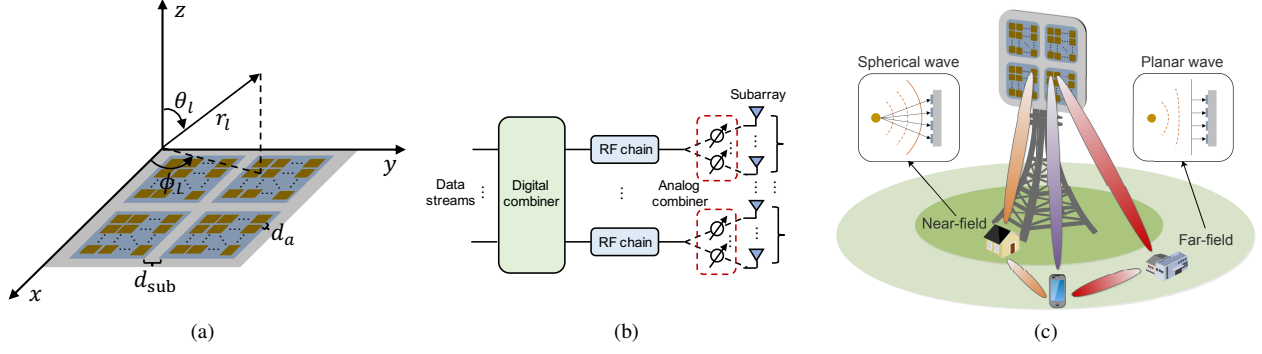


Fig. 1. System model. (a) Planar AoSA geometry of the THz UM-MIMO, in which SAs are denoted by dark blue squares while AEs are denoted by dark golden squares. (b) Partially-connected hybrid analog-digital beamforming implemented by the AoSA, where the AEs in each SA share the same RF chain through dedicated phase shifters. (c) A typical hybrid far- and near-field propagation environment in THz UM-MIMO.

pseudoinverse, trace, vectorization, and the (i, j) -th element of matrix \mathbf{A} . $\|\mathbf{a}\|_p$ and $(\mathbf{a})_i$ are the ℓ_p -norm and the i -th element of vector \mathbf{a} , respectively. $|a|$ is the absolute value of scalar a ; $\mathbf{B} = \text{blkdiag}(\mathbf{A}_1, \mathbf{A}_2, \dots, \mathbf{A}_n)$ returns a block diagonal matrix by aligning $\mathbf{A}_1, \mathbf{A}_2, \dots, \mathbf{A}_n$ along the diagonal. \mathbf{I} and $\mathbf{0}$ are the identity matrix and the all-zero vector of appropriate dimensions. $\mathbb{E}\{\cdot\}$ denotes expectation. \circ denotes the composition of functions. $\mathcal{U}(a_1, a_2)$ is a continuous uniform distribution over the interval of a_1 and a_2 . $\mathcal{CN}(\boldsymbol{\mu}, \mathbf{R})$ is a complex normal distribution with mean $\boldsymbol{\mu}$ and covariance \mathbf{R} .

II. SYSTEM MODEL AND PROBLEM FORMULATION

We consider the uplink channel estimation for THz UM-MIMO systems. The base station (BS) is equipped with a planar AoSA with $\sqrt{S} \times \sqrt{S}$ subarrays (SAs), while each SA is a uniform planar array consisting of $\sqrt{S} \times \sqrt{S}$ antenna elements (AEs), as illustrated in Fig. 1(a). To improve energy efficiency, the AoSA adopts partially-connected hybrid analog-digital beamforming [6], as shown in Fig. 1(b). Within each SA, the AEs share the same RF chain through dedicated phase shifters. A total of S RF chains are utilized to receive data streams from multiple single-antenna user equipments (UEs).

We define the index s of the SA at the m -th row and n -th column of the AoSA by $s = (m-1)\sqrt{S} + n$, where $1 \leq m, n \leq \sqrt{S}$ and $1 \leq s \leq S$. Similarly, the index \bar{s} of the AE at the \bar{m} -th row and \bar{n} -th column of a certain SA is defined by $\bar{s} = (\bar{m}-1)\sqrt{S} + \bar{n}$, where $1 \leq \bar{m}, \bar{n} \leq \sqrt{S}$ and $1 \leq \bar{s} \leq \bar{S}$. The distances between adjacent SAs and adjacent AEs are denoted by d_{sub} and d_a , respectively. As shown in Fig. 1(a), we construct a Cartesian coordinate system with the origin being the first AE in the first SA. Assuming that the AoSA lies in the x - y plane, then the coordinate of the \bar{s} -th AE in the s -th SA is given by

$$\mathbf{p}_{s, \bar{s}} = \begin{pmatrix} (m-1)[(\sqrt{S}-1)d_a + d_{\text{sub}}] + (\bar{m}-1)d_a \\ (n-1)[(\sqrt{S}-1)d_a + d_{\text{sub}}] + (\bar{n}-1)d_a \\ 0 \end{pmatrix}. \quad (1)$$

A. Hybrid-Field THz UM-MIMO Channel Model

Here we introduce the hybrid far- and near-field propagation environment along with channel model. The boundary of the far- and near-field regions is determined by the Rayleigh distance, i.e., $D_{\text{Rayleigh}} = \frac{2D^2}{\lambda_c}$, where D is the array aperture,

and λ_c is the carrier wavelength. Due to the enlarged near-field region in THz UM-MIMO, the channel can consist of both the far- and near-field paths, as shown in Fig. 1(c). The number of far- and near-field paths may vary, which renders the channel condition changeable. Additionally, since the wavefront is approximately planar in the far field and spherical in the near field, the array responses should be modeled separately.

Due to limited scattering, the spatial channel $\tilde{\mathbf{h}} \in \mathbb{C}^{S\bar{S} \times 1}$ between the BS and a specific UE can be characterized by the superposition of one LoS path and $L-1$ NLoS paths [8], i.e.,

$$\tilde{\mathbf{h}} = \gamma \sum_{l=1}^L \alpha_l \mathbf{a}(\phi_l, \theta_l, r_l) e^{-j2\pi f_c \tau_l} \quad (2)$$

where γ is a normalization factor such that $\|\tilde{\mathbf{h}}\|_2^2 = S\bar{S}$, f_c is the carrier frequency. Also, α_l , ϕ_l , θ_l , r_l , $\mathbf{a}(\phi_l, \theta_l, r_l)$, and τ_l are respectively the path loss, azimuth angle of arrival (AoA), elevation AoA, distance between the array and the RF source/scatterer, array response vector, and time delay of the l -th path. In particular, ϕ_l , θ_l , r_l are measured with respect to the origin of the coordinate system, as shown in Fig. 1(a).

1) *Path Loss*: The path loss α_l accounts for both the spread loss and the molecular absorption loss. Assuming that $l=1$ denotes the LoS path and $l>1$ denote NLoS paths, then

$$\alpha_l = |\Gamma_l| \left(\frac{c}{4\pi f_c r_1} \right) e^{-\frac{1}{2} k_{\text{abs}} r_1}, \quad (3)$$

where Γ_l is the reflection coefficient, r_1 is the LoS path length, and k_{abs} is the molecular absorption coefficient [8]. For the LoS path, $\Gamma_l = 1$. For the NLoS paths, Γ_l is given by

$$\Gamma_l = \frac{\cos \varphi_{\text{in},l} - n_t \cos \varphi_{\text{ref},l}}{\cos \varphi_{\text{in},l} + n_t \cos \varphi_{\text{ref},l}} e^{-\left(\frac{8\pi^2 f_c^2 \sigma_{\text{rough}}^2 \cos^2 \varphi_{\text{in},l}}{c^2} \right)}, \quad (4)$$

where $\varphi_{\text{in},l}$ is the angle of incidence of the l -th path, $\varphi_{\text{ref},l} = \arcsin(n_t^{-1} \sin \varphi_{\text{in},l})$ is the angle of refraction. Also, n_t and σ_{rough} are respectively the refractive index and the roughness coefficient of the reflecting material [8].

2) *Array Response Vector*: The array response vector $\mathbf{a}(\phi_l, \theta_l, r_l) \in \mathbb{C}^{S\bar{S} \times 1}$ differs in the far- and near-field regions, which are determined by the distance r_l , and is given by

$$\mathbf{a}(\phi_l, \theta_l, r_l) = \begin{cases} \mathbf{a}^{\text{far}}(\phi_l, \theta_l), & \text{if } r_l > D_{\text{Rayleigh}}, \\ \mathbf{a}^{\text{near}}(\phi_l, \theta_l, r_l) & \text{otherwise.} \end{cases} \quad (5)$$

For notational brevity, we first construct the array response matrix. Due to the planar wavefront, each element of the far-field array response matrix $\mathbf{A}^{\text{far}}(\phi_l, \theta_l)$ is

$$(\mathbf{A}^{\text{far}}(\phi_l, \theta_l))_{s,\bar{s}} = e^{-j2\pi \frac{f_c}{c} \mathbf{p}_{s,\bar{s}}^T \mathbf{t}_l}, \quad (6)$$

where c is the speed of light, and \mathbf{t}_l is the unit-length vector in the AoA direction of the l -th path, given by $\mathbf{t}_l = (\sin \theta_l \cos \phi_l, \sin \theta_l \sin \phi_l, \cos \theta_l)^T$. The corresponding far-field array response vector is given by $\mathbf{a}^{\text{far}}(\phi_l, \theta_l) = \text{vec}(\mathbf{A}^{\text{far}}(\phi_l, \theta_l))$. Due to the spherical wavefront, each element of the near-field array response matrix depends on the exact distance between the AE and the RF source/scatterer, i.e.,

$$(\mathbf{A}^{\text{near}}(\phi_l, \theta_l, r_l))_{s,\bar{s}} = e^{-j2\pi \frac{f_c}{c} \|\mathbf{p}_{s,\bar{s}} - r_l \mathbf{t}_l\|_2}. \quad (7)$$

The near-field array response vector can be similarly obtained by vectorization, i.e., $\mathbf{a}^{\text{near}}(\phi_l, \theta_l, r_l) = \text{vec}(\mathbf{A}^{\text{near}}(\phi_l, \theta_l, r_l))$.

B. Problem Formulation

In uplink channel estimation, the UEs transmit known pilot signals to the BS for Q time slots. We assume that orthogonal pilots are adopted and consider an arbitrary UE without loss of generality. For the ease of algorithm design and comparison, the spatial channel $\tilde{\mathbf{h}}$ is transformed to its angular domain representation $\bar{\mathbf{h}}$ in an SA-by-SA manner by using $\bar{\mathbf{h}} = \mathbf{F}^H \tilde{\mathbf{h}}$, where $\mathbf{F}^H = \text{blkdiag}(\mathbf{U}_1, \mathbf{U}_2, \dots, \mathbf{U}_S)$ is a unitary matrix with each \mathbf{U}_s being an $\bar{S} \times \bar{S}$ matrix constructed by the Kronecker product of two normalized discrete Fourier transform matrices of size $\sqrt{\bar{S}} \times \sqrt{\bar{S}}$. The received pilot signal $\mathbf{y}_q \in \mathbb{C}^{S \times 1}$ in the q -th time slot is given by

$$\mathbf{y}_q = \mathbf{W}_{\text{BB},q}^H \mathbf{W}_{\text{RF},q}^H \mathbf{F} \bar{\mathbf{h}} s_q + \mathbf{W}_{\text{BB},q}^H \mathbf{W}_{\text{RF},q}^H \mathbf{n}_q, \quad (8)$$

where $\mathbf{W}_{\text{BB},q} \in \mathbb{C}^{S \times S}$ is the digital combining matrix, $\mathbf{W}_{\text{RF},q} = \text{blkdiag}(\mathbf{w}_{1,q}, \mathbf{w}_{2,q}, \dots, \mathbf{w}_{S,q}) \in \mathbb{C}^{SS \times S}$ is the analog combining matrix where the elements of each component vector $\mathbf{w}_{i,q} \in \mathbb{C}^{\bar{S} \times 1}$ satisfy the constant-modulus constraint, s_q is the known pilot signal that is set as 1 for convenience, and $\mathbf{n}_q \sim \mathcal{CN}(\mathbf{0}, \sigma_n^2 \mathbf{I})$ is the noise. The average received signal-to-noise-ratio (SNR) is $\frac{1}{\sigma_n^2}$. Since the combining matrices cannot be optimally tuned without knowledge of the channel, we consider an arbitrary scenario where $\mathbf{W}_{\text{BB},q}$ is set as the identity matrix \mathbf{I} and the analog phase shifts in $\mathbf{W}_{\text{RF},q}$ are randomly chosen from one-bit quantized angles, i.e., $(\mathbf{w}_{i,q})_j \in \frac{1}{\sqrt{\bar{S}}} \{\pm 1\}$, to reduce energy consumption [11]. The received signal $\bar{\mathbf{y}} = [\mathbf{y}_1^T, \mathbf{y}_2^T, \dots, \mathbf{y}_Q^T]^T \in \mathbb{C}^{SQ \times 1}$ after Q time slots of pilot transmission is given by

$$\bar{\mathbf{y}} = \bar{\mathbf{M}} \bar{\mathbf{h}} + \bar{\mathbf{n}}, \quad (9)$$

where $\bar{\mathbf{M}} = [(\mathbf{W}_{\text{RF},1}^H \mathbf{F})^T, \dots, (\mathbf{W}_{\text{RF},Q}^H \mathbf{F})^T]^T \in \mathbb{C}^{SQ \times SS}$, and $\bar{\mathbf{n}} = [(\mathbf{W}_{\text{RF},1}^H \mathbf{n}_1)^T, \dots, (\mathbf{W}_{\text{RF},Q}^H \mathbf{n}_Q)^T]^T \in \mathbb{C}^{SQ \times 1}$.

To transform (9) into its equivalent real-valued form, we let $\mathbf{y} = [\Re(\bar{\mathbf{y}})^T, \Im(\bar{\mathbf{y}})^T]^T \in \mathbb{R}^{2SQ \times 1}$, $\mathbf{h} = [\Re(\bar{\mathbf{h}})^T, \Im(\bar{\mathbf{h}})^T]^T \in \mathbb{R}^{2SS \times 1}$, $\mathbf{n} = [\Re(\bar{\mathbf{n}})^T, \Im(\bar{\mathbf{n}})^T]^T \in \mathbb{R}^{2SQ \times 1}$, and

$$\mathbf{M} = \begin{pmatrix} \Re(\bar{\mathbf{M}}) & -\Im(\bar{\mathbf{M}}) \\ \Im(\bar{\mathbf{M}}) & \Re(\bar{\mathbf{M}}) \end{pmatrix} \in \mathbb{R}^{2SQ \times 2SS}. \quad (10)$$

Then, the equivalent real-valued form is given by

$$\mathbf{y} = \mathbf{M} \mathbf{h} + \mathbf{n}. \quad (11)$$

Based on (11), channel estimation can be formulated as a linear inverse problem whose goal is to compute a good estimate of \mathbf{h} given the knowledge of \mathbf{y} and \mathbf{M} . However, due to the practical requirements of low pilot overhead and limited RF chains, it is often the case that $SQ \ll SS$, which makes the problem significantly ill-posed. Existing works rely heavily on the channel sparsity to design compressed sensing algorithms for channel estimation. However, the sparsifying transformations for the far- and near-field paths are not compatible with each other [10]. DU methods could be adopted but they generally lack theoretical guarantees. Additionally, the *fixed* number of layers limits their ability to adapt to the changeable channel conditions and can cause unstable performance. These drawbacks motivate us to design an efficient deep learning based hybrid-field channel estimator with provable convergence guarantee and adaptive complexity.

III. FIXED POINT NETWORKS FOR HYBRID-FIELD THZ UM-MIMO CHANNEL ESTIMATION

A. Fixed Point Modeling of Neural Networks

Most iterative algorithms for solving linear inverse problems can be represented in the following general form, i.e.,

$$\mathbf{h}^{(t+1)} = f_{\Theta}(\mathbf{h}^{(t)}; \mathbf{y}), \quad (12)$$

where $\mathbf{h}^{(t)}$ denotes the intermediate estimation at the t -th iteration, and f_{Θ} denotes a mapping parameterized by Θ . Well-known examples of this general form include proximal algorithms, OAMP, and also weight-tied neural networks. The limit as $t \rightarrow \infty$, i.e., \mathbf{h}^* , supposed that it exists, is a solution of the fixed point equation

$$\mathbf{h}^* = f_{\Theta}(\mathbf{h}^*; \mathbf{y}), \quad (13)$$

which models the behavior of an algorithm at its convergence. Particularly, if $f_{\Theta}(\cdot; \mathbf{y})$ corresponds to one layer of a weight-tied neural network, then the fixed point \mathbf{h}^* is the output of the network after an *infinite* number of layers [18], [19].

Our basic idea is to design a neural network assisted mapping $f_{\Theta}(\cdot; \mathbf{y})$ such that its fixed point is a good estimate of the hybrid-field channel given the pilot measurement \mathbf{y} . We refer to such a general framework as the *fixed point network* (FPN). Specifically, $f_{\Theta}(\cdot; \mathbf{y})$ can be constructed by adding learnable components to various different algorithms that belong to (12). The remaining question is how we can ensure the existence of the fixed point and find it efficiently. Before further discussion, we first define two key concepts.

Definition 1 (Lipschitz continuity). A mapping $f_{\Theta}(\cdot; \mathbf{y})$ is Lipschitz continuous if there exists a constant L such that

$$\|f_{\Theta}(\mathbf{h}_1; \mathbf{y}) - f_{\Theta}(\mathbf{h}_2; \mathbf{y})\| \leq L \|\mathbf{h}_1 - \mathbf{h}_2\|$$

holds for any $\mathbf{h}_1, \mathbf{h}_2 \in \text{dom}(f_{\Theta}(\cdot; \mathbf{y}))$.

Definition 2 (Contractive). A mapping $f_{\Theta}(\cdot; \mathbf{y})$ is contractive if it is Lipschitz continuous with constant $0 \leq L < 1$.

The existence of the fixed point and an efficient way to find it can both be ensured by fixed point theory. As long as $f_{\Theta}(\cdot; \mathbf{y})$

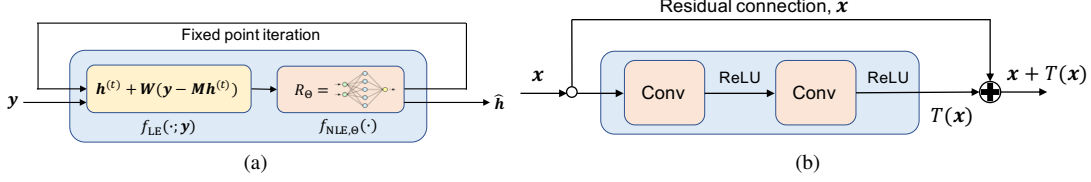


Fig. 2. (a) The schematic diagram of the proposed FPN-OAMP. (b) The structure of one residual block. Let the input be \mathbf{x} , then the output is $\mathbf{x} + T(\mathbf{x})$.

is a contractive mapping (no matter what detailed operations it contains), a simple repeated application of $f_{\Theta}(\cdot; \mathbf{y})$ will make $\mathbf{h}^{(t)}$ converge linearly to the unique fixed point \mathbf{h}^* .

Theorem 3 (Banach-Picard [16, Theorem 1.50]). *For any initial value $\mathbf{h}^{(0)}$, if the sequence $\{\mathbf{h}^{(t)}\}$ is generated via the relation $\mathbf{h}^{(t+1)} = f_{\Theta}(\mathbf{h}^{(t)}; \mathbf{y})$ and $f_{\Theta}(\cdot; \mathbf{y})$ is a contractive mapping with Lipschitz constant $0 \leq L < 1$, then $\{\mathbf{h}^{(t)}\}$ converges to the unique fixed point \mathbf{h}^* of $f_{\Theta}(\cdot; \mathbf{y})$ with a linear convergence rate L . The gap between $\mathbf{h}^{(t)}$ and \mathbf{h}^* decreases geometrically as $\|\mathbf{h}^{(t+1)} - \mathbf{h}^*\|_2 \leq L\|\mathbf{h}^{(t)} - \mathbf{h}^*\|_2$.*

This theorem reveals several unique advantages of the FPNs that are not available in prevailing DU methods. First, it provides a simple and unified framework to establish convergence guarantee. The only requirement, i.e., $f_{\Theta}(\cdot; \mathbf{y})$ is contractive, can be satisfied by controlling the Lipschitz constant of the neural network during training [20]. Second, the complexity of FPNs is adaptive and can be adjusted at the testing time. Since the fixed point iteration converges linearly to the unique fixed point \mathbf{h}^* , one can run it to an arbitrary depth depending on the desired accuracy and the hybrid-field channel condition (reflected in \mathbf{y}). This will offer a flexible tradeoff between complexity and performance, as well as an excellent ability to adapt to the changeable channel conditions.

B. FPN-OAMP

As mentioned before, there are a lot of possible choices for the mapping f_{Θ} . To incorporate wireless domain knowledge, we design it based on the algorithmic structure of a powerful compressed sensing algorithm, i.e., the OAMP. The proposed FPN-based variant of it, called the FPN-OAMP, consists of a closed-form linear estimator (LE) and a CNN-based nonlinear estimator (NLE). The mapping $f_{\Theta}(\cdot; \mathbf{y})$ is a composition of them, i.e., $f_{\Theta}(\cdot; \mathbf{y}) = (f_{\text{NLE}, \Theta} \circ f_{\text{LE}})(\cdot; \mathbf{y})$. The process of FPN-OAMP is summarized in Fig. 2(a) and Algorithm 1.

1) *Linear Estimator*: The LE of FPN-OAMP is similar to that of OAMP. It is given by

$$f_{\text{LE}}(\mathbf{h}^{(t)}; \mathbf{y}) = \mathbf{h}^{(t)} + \mathbf{W}(\mathbf{y} - \mathbf{M}\mathbf{h}^{(t)}). \quad (14)$$

The LE matrix $\mathbf{W} \in \mathbb{R}^{2S\bar{S} \times 2SQ}$ is constructed by¹

$$\mathbf{W} = \eta \mathbf{M}^{\dagger} = \frac{2S\bar{S}}{\text{tr}(\mathbf{M}^{\dagger} \mathbf{M})} \mathbf{M}^{\dagger}, \quad (15)$$

where η is the step size that ensures $\text{tr}(\mathbf{I} - \mathbf{W}\mathbf{M}) = 0$, such that the LE is de-correlated [17].

¹The measurement matrix \mathbf{M} is fixed since the combining matrices cannot be optimally tuned without knowledge of the channel [11]. As a result, the LE matrix \mathbf{W} is fixed, and thus the computation of pseudoinverse is avoided.

2) *Nonlinear Estimator*: The NLE is given by

$$f_{\text{NLE}, \Theta}(f_{\text{LE}}(\mathbf{h}^{(t)}; \mathbf{y})) = R_{\Theta}(f_{\text{LE}}(\mathbf{h}^{(t)}; \mathbf{y})), \quad (16)$$

where $R_{\Theta}(\cdot)$ is a ResNet-like structure consisting of three residual blocks (RBs), as shown in Fig. 2(b). Before the RBs, $f_{\text{LE}}(\mathbf{h}^{(t)}; \mathbf{y})$ is first reshaped into a tensor of S feature maps of size $\sqrt{S} \times \sqrt{S}$, each corresponding to an SA, and then passes through a convolution (Conv) layer to lift them to 64 feature maps. Each RB constitutes two Conv layers with 3×3 kernels and a fixed number of 64 feature maps, which are respectively followed by a ReLU activation. We further follow the RBs by two 1×1 Conv layers, where the first one adopts leaky ReLU activation, before reshaping back to the vector form $\mathbf{h}^{(t+1)}$.

Algorithm 1 FPN-OAMP for hybrid-field channel estimation

- 1: **Input**: Measurement matrix \mathbf{M} , received pilot signals \mathbf{y} , weights of the nonlinear estimator Θ , error tolerance ϵ
- 2: **Output**: Estimated hybrid-field THz channel $\hat{\mathbf{h}}$
- 3: **Initialize**: $\mathbf{h}^{(0)} \leftarrow \mathbf{0}, t \leftarrow 0$
- 4: Fixed point iteration of $(f_{\text{NLE}, \Theta} \circ f_{\text{LE}})(\cdot; \mathbf{y})$:
- 5: **while** $\|\mathbf{h}^{(t)} - (f_{\text{NLE}, \Theta} \circ f_{\text{LE}})(\mathbf{h}^{(t)}; \mathbf{y})\|_2 > \epsilon$ **do**
- 6: $\mathbf{h}^{(t+1)} \leftarrow (f_{\text{NLE}, \Theta} \circ f_{\text{LE}})(\mathbf{h}^{(t)}; \mathbf{y})$
- 7: $t \leftarrow t + 1$
- 8: $\hat{\mathbf{h}} \leftarrow \mathbf{h}^{(t)}$
- 9: **return** $\hat{\mathbf{h}}$

C. Linear Convergence of the FPN-OAMP

To prove the linear convergence of the FPN-OAMP, on the basis of Theorem 3, we need to show that $(f_{\text{NLE}, \Theta} \circ f_{\text{LE}})(\cdot; \mathbf{y})$ is contractive, which is proved as follows.

Lemma 4 ([20]). *The composition of an L_1 -Lipschitz and an L_2 -Lipschitz mapping is $L_1 L_2$ -Lipschitz.*

Theorem 5. *Each layer of the FPN-OAMP $(f_{\text{NLE}, \Theta} \circ f_{\text{LE}})(\cdot; \mathbf{y})$ is a contractive mapping if $R_{\Theta}(\cdot)$ is contractive.*

Proof: We begin by showing that the Lipschitz constant of $f_{\text{LE}}(\cdot; \mathbf{y})$ is 1. Because the non-zero eigenvalues of $\mathbf{M}^{\dagger} \mathbf{M}$ and $\mathbf{M} \mathbf{M}^{\dagger} = \mathbf{I}$ are the same, the eigenvalues of $\mathbf{M}^{\dagger} \mathbf{M}$ equal either 0 or 1. Since $f_{\text{LE}}(\cdot; \mathbf{y})$ is an affine mapping, its Lipschitz constant is the spectral norm of $\mathbf{I} - \eta \mathbf{M}^{\dagger} \mathbf{M}$, i.e., the largest singular value of the matrix, given by

$$\text{Lip}(f_{\text{LE}}(\cdot; \mathbf{y})) = \max_i (1 - \eta \lambda_i(\mathbf{M}^{\dagger} \mathbf{M})) = 1, \quad (17)$$

where $\lambda_i(\cdot)$ denotes the i -th eigenvalue of a matrix. Therefore, according to Lemma 4, the composition $(f_{\text{NLE}, \Theta} \circ f_{\text{LE}})(\cdot; \mathbf{y})$ is a contractive mapping if $R_{\Theta}(\cdot)$ is contractive. ■

Remark 6. We provide details on training a contractive $R_\Theta(\cdot)$ afterwards. Since $(f_{\text{NLE},\Theta} \circ f_{\text{LE}})(\cdot; \mathbf{y})$ is contractive regardless of \mathbf{y} , the linear convergence rate of FPN-OAMP will hold for different channel conditions and SNR levels. The error tolerance ϵ in **Algorithm 1** explicitly controls the accuracy of the approximate fixed point $\hat{\mathbf{h}}$, since the gap between $\mathbf{h}^{(t)}$ and \mathbf{h}^* decreases geometrically. Adjusting ϵ can provide a flexible tradeoff between complexity and performance.

D. Training of the FPN-OAMP

During training, we first run the fixed point iteration to find the approximate fixed point $\hat{\mathbf{h}}$ given an error tolerance ϵ . The loss function is chosen as the normalized mean squared error (NMSE) of $\hat{\mathbf{h}}$ and the ground truth channel \mathbf{h} , i.e.,

$$\ell(\hat{\mathbf{h}}, \mathbf{h}) \triangleq \mathbb{E}\{\|\mathbf{h} - \hat{\mathbf{h}}\|_2^2 / \|\mathbf{h}\|_2^2\}. \quad (18)$$

We adopt the Jacobian-free backpropagation in [19] to train the FPN-OAMP, which only imposes a *constant* memory overhead regardless of the number of fixed point iterations. To enforce the contractive property of $R_\Theta(\cdot)$, we check its Lipschitz constant after each weight update using the current batch of training data. The Lipschitz constant is approximated by

$$L = \frac{\sum_{i=1}^B \|R_\Theta(\hat{\mathbf{h}}_i + \delta_i; \mathbf{y}) - R_\Theta(\hat{\mathbf{h}}_i; \mathbf{y})\|_2}{\sum_{i=1}^B \|\delta_i\|_2}, \quad (19)$$

where B is the batch size, $\hat{\mathbf{h}}_i$ corresponds to the i -th training sample, and δ_i is a small random perturbation [21]. According to **Lemma 4**, since the LE and the (leaky) ReLU activations in the NLE are all 1-Lipschitz [20], the Lipschitz constant of $(f_{\text{NLE},\Theta} \circ f_{\text{LE}})(\cdot; \mathbf{y})$ is only determined by the Conv layers. Additionally, since each Conv layer is an affine mapping, its Lipschitz constant is the spectral norm of the weight matrix, which can be controlled by multiplying the weight by a constant. Therefore, if the contractive property is found violated, i.e., $L \geq 1$, we can correct it by replacing the weights of each Conv layer in R_Θ , i.e., Θ , by $(\beta/L)^{\frac{1}{2}}\Theta$, where $0 \leq \beta < 1$ is the desired Lipschitz constant of the NLE².

IV. SIMULATION RESULTS

This section provides simulation results to evaluate the performance of the proposed FPN-OAMP method in a typical THz UM-MIMO system [8]. The key simulation parameters are summarized in Table I. Specifically, r_l is set as a random variable spanning both far- and near-field regions to model the hybrid-field propagation. The performance metric is the NMSE, which is averaged over a testing dataset with 5000 samples. Five benchmarks are adopted for comparison:

- **LS**: Least squares.
- **OMP**: Orthogonal matching pursuit [7], [8], [10].
- **OAMP**: OAMP with the pseudoinverse LE [17].
- **FISTA**: Fast iterative soft thresholding algorithm [22].
- **ISTA-Net+**: State-of-the-art DU method based on the iterative soft thresholding algorithm [23]. The number of layers is fixed as 10, since a further increase is observed to offer only negligible performance gain.

²The exponent $\frac{1}{2}$ is chosen because $R_\Theta(\cdot)$ has 9 Conv layers in total. Although there are residual connections in the RBs, [21] has shown that the Lipschitz constant can still be controlled in this way, as long as β/L is close to 1, i.e., the contractive property is not seriously violated. Actually, we observed that the correction was seldom triggered during training.

TABLE I
KEY SIMULATION PARAMETERS

Parameter	Value
Number of SAs / RF chains	$S = 4$
Number of AEs per SA	$\bar{S} = 256$
Number of BS antennas	$\bar{S} = 1024$
Carrier frequency	$f_c = 300$ GHz
AE spacing	$d_a = 5.0 \times 10^{-4}$ m
SA spacing	$d_{\text{sub}} = 5.6 \times 10^{-2}$ m
Pilot length	$Q = 128$
Azimuth AoA	$\theta_l \sim \mathcal{U}(-\pi/2, \pi/2)$
Elevation AoA	$\phi_l \sim \mathcal{U}(-\pi, \pi)$
Angle of incidence	$\varphi_{\text{in},l} \sim \mathcal{U}(0, \pi/2)$
Number of paths	$L = 5$
Rayleigh distance	$D_{\text{Rayleigh}} = 20$ m
LoS path length	$r_1 = 30$ m
Scatterer distance ($l > 1$)	$r_l \sim \mathcal{U}(10, 25)$ m
Time delay of LoS path	$\tau_1 = 100$ nsec
Time delay of NLoS paths ($l > 1$)	$\tau_l \sim \mathcal{U}(100, 110)$ nsec
Absorption coefficient	$k_{\text{abs}} = 0.0033$ m ⁻¹
Refractive index	$n_t = 2.24 - j0.025$
Roughness factor	$\sigma_{\text{rough}} = 8.8 \times 10^{-5}$ m

We train two different sets of parameters for both ISTA-Net+ and the proposed FPN-OAMP: one for the low SNR scenario (0 to 10 dB), and the other for the high SNR scenario (10 to 20 dB). For each scenario, we generate 80000, 5000, and 5000 samples for the purpose of training, validation, and testing, respectively. The SNR of each sample is randomly drawn based on its respective scenario. We train the networks for 150 epochs using the Adam optimizer with an initial learning rate of 0.001 and a batch size of 128. The learning rate is reduced by half after every 30 epochs. When training the FPN-OAMP, we set the error tolerance ϵ as 0.01 and the maximum number of iteration as 15 to accelerate the process. Note that in the testing stage, FPN-OAMP can run for an arbitrary number of iterations, depending on the channel condition and the error tolerance ϵ . For fair comparison with ISTA-Net+, during testing, we also set the error tolerance as 0.01, and the maximum number of iterations as 15.

In Fig. 3(a), we present the NMSE performance versus the average received SNR. It is observed that the proposed FPN-OAMP significantly outperforms all five benchmarks under different SNR levels. Compared with its base algorithm OAMP, the performance gain of FPN-OAMP is as large as about 15 dB in terms of NMSE. This indicates that the CNN component of FPN-OAMP can effectively identify and exploit the complicated hybrid-field channel conditions.

In Fig. 3(b), we illustrate the NMSE evaluated at different iteration/layer t when SNR = 5 dB. LS and OMP are not plotted since they do not produce intermediate results. As observed, NMSE of the proposed FPN-OAMP and its base algorithm OAMP converges rapidly within only 4 iterations, while FISTA converges after about 20 iterations. Notably, the performance of FPN-OAMP at iteration 2 has already outperformed the final performance of all benchmark methods, which demonstrates its superior efficiency. By contrast, the intermediate performance of the DU method, ISTA-Net+, is very unstable and keeps fluctuating until layer 7. This is because DU is a black-box solver which only seeks to optimize the final estimation quality but does not explicitly control the internal dynamics like the proposed FPN-OAMP. Additionally, the fixed number

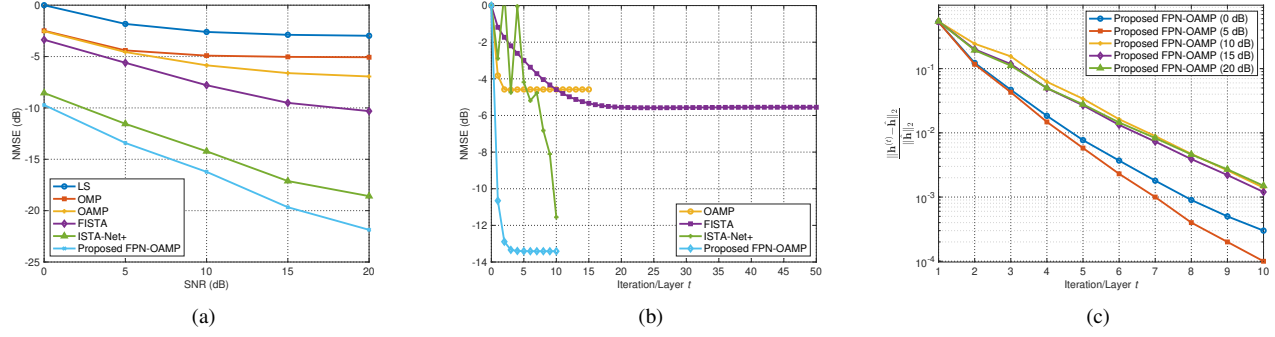


Fig. 3. Simulation results. (a) NMSE performance versus SNR. (b) NMSE evaluated at iteration/layer t when SNR = 5 dB. (c) Normalized gap between the intermediate estimate at iteration/layer t and the approximate fixed point of the proposed FPN-OAMP.

of layers limits its ability to adapt to the changeable hybrid-field channel conditions.

Fig. 3(c) provides numerical verifications for the linear convergence of FPN-OAMP under different SNR levels. In logarithmic scale, we plot the normalized gap between the intermediate estimate at iteration/layer t , i.e., $\mathbf{h}^{(t)}$, and the approximate fixed point, i.e., $\hat{\mathbf{h}}$, defined by $\|\mathbf{h}^{(t)} - \hat{\mathbf{h}}\|_2 / \|\hat{\mathbf{h}}\|_2$. It is observed that the curves are all linear, which demonstrates that the linear convergence property identified in Subsection III-C is consistent under different SNR levels, and the training strategy presented in Subsection III-D is effective. Although we plot the averaged results over the testing dataset for illustration, it is worth noting that the linear convergence property holds for each individual sample.

V. CONCLUSIONS AND FUTURE WORK

In this paper, we proposed an efficient deep learning based hybrid-field channel estimator for THz UM-MIMO. Significant performance gains are then observed in comparison with state-of-the-art benchmarks. One unique advantage is the linear convergence guarantee based on fixed point theory, which is not available in the prevailing DU methods. Besides, the computational complexity is adaptive, making it more suitable for future wireless networks with complicated hybrid-field channel conditions. Further extension of the proposed FPNs to other important inverse problems in wireless communications, such as data detection, is a promising future direction.

REFERENCES

- [1] H. Sarieddeen, M.-S. Alouini, and T. Y. Al-Naffouri, "An overview of signal processing techniques for terahertz communications," *Proc. IEEE*, vol. 109, no. 10, pp. 1628–1665, Oct. 2021.
- [2] I. F. Akylidiz, C. Han, Z. Hu, S. Nie, and J. M. Jornet, "Terahertz band communication: An old problem revisited and research directions for the next decade," *IEEE Trans. Commun.*, vol. 70, no. 6, pp. 4250–4285, Jun. 2022.
- [3] K. B. Letaief, Y. Shi, J. Lu, and J. Lu, "Edge artificial intelligence for 6G: Vision, enabling technologies, and applications," *IEEE J. Sel. Areas Commun.*, vol. 40, no. 1, pp. 5–36, Jan. 2022.
- [4] B. Ning, Z. Chen, Z. Tian, C. Han, and S. Li, "A unified 3D beam training and tracking procedure for terahertz communication," *IEEE Trans. Wireless Commun.*, vol. 21, no. 4, pp. 2445–2461, Apr. 2022.
- [5] X. Yu, J.-C. Shen, J. Zhang, and K. B. Letaief, "Alternating minimization algorithms for hybrid precoding in millimeter wave MIMO systems," *IEEE J. Sel. Top. Signal Process.*, vol. 10, no. 3, pp. 485–500, Apr. 2016.
- [6] J. Zhang, X. Yu, and K. B. Letaief, "Hybrid beamforming for 5G and beyond millimeter-wave systems: A holistic view," *IEEE Open J. Commun. Soc.*, vol. 1, pp. 77–91, Jan. 2020.
- [7] J. Lee, G.-T. Gil, and Y. H. Lee, "Channel estimation via orthogonal matching pursuit for hybrid MIMO systems in millimeter wave communications," *IEEE Trans. Commun.*, vol. 64, no. 6, pp. 2370–2386, Jun. 2016.
- [8] K. Dovelos, M. Matthaiou, H. Q. Ngo, and B. Bellalta, "Channel estimation and hybrid combining for wideband terahertz massive MIMO systems," *IEEE J. Sel. Areas Commun.*, vol. 39, no. 6, pp. 1604–1620, Jun. 2021.
- [9] Y. Han, S. Jin, C.-K. Wen, and X. Ma, "Channel estimation for extremely large-scale massive MIMO systems," *IEEE Wireless Commun. Lett.*, vol. 9, no. 5, pp. 633–637, May 2020.
- [10] X. Wei and L. Dai, "Channel estimation for extremely large-scale massive MIMO: Far-field, near-field, or hybrid-field?" *IEEE Commun. Lett.*, vol. 26, no. 1, pp. 177–181, Jan. 2022.
- [11] H. He, C.-K. Wen, S. Jin, and G. Y. Li, "Deep learning-based channel estimation for beamspace mmWave massive MIMO systems," *IEEE Wireless Commun. Lett.*, vol. 7, no. 5, pp. 852–855, Oct. 2018.
- [12] H. He, S. Jin, C.-K. Wen, F. Gao, G. Y. Li, and Z. Xu, "Model-driven deep learning for physical layer communications," *IEEE Wireless Commun.*, vol. 26, no. 5, pp. 77–83, Oct. 2019.
- [13] H. He, C.-K. Wen, S. Jin, and G. Y. Li, "Model-driven deep learning for MIMO detection," *IEEE Trans. Signal Process.*, vol. 68, pp. 1702–1715, Feb. 2020.
- [14] Y. Ma, Y. Shen, X. Yu, J. Zhang, S. H. Song, and K. B. Letaief, "Learn to communicate with neural calibration: Scalability and generalization," *IEEE Trans. Wireless Commun.*, to appear.
- [15] Y. Shen, J. Zhang, and K. B. Letaief, "How neural architectures affect deep learning for communication networks?" in *Proc. IEEE Int. Conf. Commun. (ICC)*, May 2022.
- [16] H. H. Bauschke and P. L. Combettes, *Convex analysis and monotone operator theory in Hilbert spaces (2nd edition)*. Springer, 2019.
- [17] J. Ma and L. Ping, "Orthogonal AMP," *IEEE Access*, vol. 5, pp. 2020–2033, Jan. 2017.
- [18] S. Bai, J. Z. Kolter, and V. Koltun, "Deep equilibrium models," in *Proc. Adv. Neural Inf. Process. Syst. (NeurIPS)*, Dec. 2019.
- [19] S. W. Fung, H. Heaton, Q. Li, D. McKenzie, S. Osher, and W. Yin, "JFB: Jacobian-free backpropagation for implicit models," in *Proc. Assoc. Adv. Artif. Intell. (AAAI)*, Feb. 2022.
- [20] H. Gouk, E. Frank, B. Pfahringer, and M. J. Cree, "Regularisation of neural networks by enforcing Lipschitz continuity," *Mach. Learn.*, vol. 110, no. 2, pp. 393–416, Dec. 2021.
- [21] H. Heaton, S. W. Fung, A. Gibali, and W. Yin, "Feasibility-based fixed point networks," *Fixed Point Theory Algorithms Sci. Eng.*, vol. 2021, no. 1, pp. 1–19, Nov. 2021.
- [22] A. Beck and M. Teboulle, "A fast iterative shrinkage-thresholding algorithm for linear inverse problems," *SIAM J. Imaging Sci.*, vol. 2, no. 1, pp. 183–202, Feb. 2009.
- [23] J. Zhang and B. Ghanem, "ISTA-Net: Interpretable optimization-inspired deep network for image compressive sensing," in *Proc. IEEE/CVF Conf. Comput. Vis. Pattern Recognit. (CVPR)*, Jun. 2018.